Bio-Design and Manufacturing (2021) 4:452–468
https://doi.org/10.1007/s42242-021-00130-x

RESEARCH ARTICLE

A bifunctional bone scaffold combines osteogenesis and antibacterial activity via in situ grown hydroxyapatite and silver nanoparticles

Youwen Yang[1,2] · Yun Cheng[1] · Fang Deng[1] · Lida Shen[2] · Zhenyu Zhao[3] · Shuping Peng[4,5] · Cijun Shuai[1,3,6]

Received: 14 December 2020 / Accepted: 4 March 2021 / Published online: 23 March 2021

Abstract

Hydroxyapatite (HA) nanoparticles and silver (Ag) nanoparticles are expected to enable desirable bioactivity and antibacterial properties on biopolymer scaffolds. Nevertheless, interfacial adhesion between HA/Ag and the biopolymer is poor due to the large physicochemical differences between these components. In this study, poly L-lactic acid (PLLA) powder was first surface-modified with bioactive polydopamine (PDA) in an alkaline environment. Next, HA and Ag nanoparticles were grown in situ on the PDA-coated PLLA powder, which was then adhered to the porous bone scaffold using a selective laser-sintering process. Results showed that HA and Ag nanoparticles were homogenously distributed in the matrix, with enhanced mechanical properties. Simulated body fluid bioactivity tests showed that the in situ grown HA-endowed scaffold shows excellent bioactivity. In vitro tests confirmed that the scaffold exhibits favorable biocompatibility with human umbilical cord mesenchymal stem cells, as well as strong antibacterial activity against Gram-negative *Escherichia coli*. Furthermore, in vivo assays indicated that the scaffold promoted bone generation, with a new bone area fraction of 71.8% after 8 weeks' implantation, without inflammation.

Keywords Bone scaffold · In situ growth · Hydroxyapatite · Antibacterial properties · Surface modification

Introduction

Bone scaffolds play a key role in clinical repair of bone defects [1–4]. Biopolymers such as poly L-lactic acid (PLLA), polyglycolide and polycaprolactone are considered promising bone scaffold materials because of their good biocompatibility, natural biodegradability, as well as favorable processability [5, 6]. Unfortunately, these biopolymers lack bioactivity, with excessively slow bone growth at the scaffold/tissue interface [7]. In addition, bacterial infection often occurs during implantation surgery, a problem that can result in bone repair failure [8, 9].

Incorporating bioceramic nanoparticles such as hydroxyapatite (HA) to form organic/inorganic composite with compositional analogies to natural bone is an available method to gain the desirable levels of bioactivity, while introduction of silver (Ag) nanoparticles has been shown to add antibacterial properties [10–12]. Nevertheless, interfacial compatibility between the polymer matrix and nanoparticles (including HA and Ag) is rather poor due to the large physicochemical differences between these components, which results in weak interfacial adhesion [13, 14]. Meanwhile, nanoparticles possess high specific-surface and high

✉ Shuping Peng
shuping@csu.edu.cn

✉ Cijun Shuai
shuai@csu.edu.cn

1 Institute of Bioadditive Manufacturing, Jiangxi University of Science and Technology, Nanchang 330013, China

2 Jiangsu Key Laboratory of Precision and Micro-Manufacturing Technology, Nanjing University of Aeronautics and Astronautics, Nanjing 210016, China

3 Shenzhen Institute of Information Technology, Shenzhen 518172, China

4 NHC Key Laboratory of Carcinogenesis, School of Basic Medical Science, Central South University, Changsha 410013, China

5 School of Energy and Machinery Engineering, Jiangxi University of Science and Technology, Nanchang 330013, China

6 State Key Laboratory of High Performance Complex Manufacturing, Central South University, Changsha 410083, China

surface energy [15]. As a consequence, nanoparticles tend to aggregate in the polymer matrix, inevitably reducing the composite performance [16].

In situ generation technology shows great potential in improving interface adhesion and dispersion state of the incorporated nanoparticles [17]. Surface modification is generally required to obtain in situ grown nanoparticles, a process that can create active in situ growth sites through grafting a large number of functional groups on the matrix surface. For example, Zhu et al. reported gold nanoparticles successfully grown in situ on Fe_3O_4 modified by tetraethyl orthosilicate, which exhibited a good bonding interface and uniform distribution state [18]. Zhang et al. achieved in situ growth of SiO_2 nanoparticles on polyethersulfone powder coated with polydopamine (PDA), which also presented uniform distribution state [19].

An undeniable fact is that surface modifiers play a key role in the in situ growth of nanoparticles [20]. PDA, a mussel-inspired adhesive material formed by oxidative polymerization of dopamine (DA), can strongly adhere to a variety of substrates due to its large content of active catechol and amine groups [21]. Significantly, PDA can absorb Ca^{2+} by chelation in simulated body fluid (SBF) and then absorb HPO_4^{2-} through electrostatic interaction, thus achieving the in situ nucleation of HA [22]. Meanwhile, the catechol groups on PDA have weak reducibility and can reduce some metal ions into nanoparticles, including Ag [23], gold [24] and platinum [25]. Specifically, previous researchers have achieved in situ growth of Ag nanoparticles on PDA-coated scaffolds in Ag^+ solution.

In this study, we adopted in situ generation technology to introduce HA and Ag nanoparticles to a biopolymer scaffold. First, PLLA powder was surface-modified using PDA. Next, HA and Ag nanoparticles were grown in situ on the modified PLLA powder in SBF and $AgNO_3$ solution, respectively. Finally, the composite powder was developed into scaffolds by selective laser-sintering (SLS) technology. SLS, as one representative additive manufacturing process, was able to fabricate a complicated porous structure with the aid of computer aided design (CAS). In recent years, SLS has been applied to processing a wide range of biomaterials, including metals [26–28], ceramics [29], and polymers [30] and their composites [31], exhibiting the great potential of this process for biomedical application. The microstructural features, bioactivity, and antibacterial activity of the scaffold structures were comprehensively studied. In vitro biocompatibility and in vivo osteogenesis were also investigated in this material, with the aim of achieving an overall evaluation for clinical applications of bone tissue engineering.

Materials and methods

Raw materials

The original PLLA powder was obtained from Shenzhen Polymtek Biomaterial Co., Ltd. (Shenzhen, China). Ag nitrate was obtained from Sinopharm Chemical Reagent Co., Ltd. DA hydrochloride, Tris-HCl solution, fetal bovine serum (FBS), phosphate-buffered saline (PBS), Dulbecco's modified Eagle's medium (DMEM), calcein-acetoxymethylester (calcein-AM), ethidium homodimer-1 reagent, penicillin, and streptomycin were obtained from Sigma-Aldrich (Shanghai, China). All the reagents were analytically pure.

In situ growth and scaffold preparation

PLLA as a template was first surface-modified by PDA. In detail, PLLA powder (1 g) and dopamine hydrochloride (60 mg) were mixed in 30 mL of Tris-HCl solution (10 mM, pH 8.5) using magnetic stirring for 6 h. The mixture was then centrifuged 10 min at 8000 r/min. The resulting precipitate (modified PLLA) was washed and dried for 6 h. The modified PLLA powder was immersed into 100 mL of 1.5 × SBF solution at 37 °C for 3 days, with the immersion solution renewed every day. The ion concentration of 1.5 × SBF was 1.5 times of that in SBF. In this condition, HA nanoparticles were expected to grow in situ on modified PLLA powder. Afterward, the HA_modified powder ("PLLA@HA") was collected and dried at 40 °C for 1 day. The PLLA@HA powder was added into an $AgNO_3$ solution (50 mM) and magnetically stirred for 5 h. Afterward, the resulting powder ("PLLA@HA@Ag") was collected and dried for scaffold preparation.

Porous scaffolds with a diameter of 4 mm and length of 15 mm were manufactured using an in-house-created SLS system composed of a carbon dioxide laser (50 W), a powder delivery system, and a computer system for process control. The process parameters were optimized after a series of preliminary experiments and were set as follows: laser power 2.3 W, scanning rate 100 mm/s, thickness 0.1 mm, and scan space 1 mm. The laser spot size was about 300 μm. During SLS, high-purity nitrogen was used to prevent oxidation of PLLA powder.

Microstructural and mechanical characterization

The chemical composition of PLLA@HA@Ag powder was determined by X-ray photoelectron spectroscopy (XPS,

ThermoFisher-VG Scientific, UK) with Al Kα radiation (1486.6 eV, line width 0.7 eV). During spectra recording, the energy resolution was regulated at 0.4 eV. The phase composition was investigated with an X-ray diffractometer (XRD, D8 Advance, Bruker Co., Germany) with Cu Kα radiation at 40 kV and 150 mA. The scanning range was 10°-80°, and the scanning rate was 8°/min. Particle size distribution was investigated using a laser particle size analyzer (Mastersizer 3000, Malvern Instruments Ltd., UK). Before testing, 100 mg of powder was dispersed in 1 mL of absolute ethanol and then stirred at 2000 r/min. Subsequently, the suspension was loaded in the analyzer for determination. The powder was investigated using transmission electron microscopy (TEM, FEI, USA).

The scaffold surface was examined under a scanning electron microscope (SEM, EVO 18, ZEISS, Germany) equipped with energy-dispersive spectroscopy (EDS, X-Max 20, Oxford Instruments, UK). Surface hydrophilicity was measured using an optical tensiometer (Attension Theta, Biolin Scientific Ltd., Sweden). One drop of water (about 5 μL) was released onto the scaffold surface via an automatic precision syringe. The angle between the scaffold surface and the tangent of the drop was then determined. The compressive properties of the scaffolds were evaluated by a testing system (Metes industrial systems Co. Ltd., China) using a loading rate of 1 mm/min. Hardness was tested on a microhardness tester (Beijing TIME High Technology Co. Ltd., China) at a load of 9.8 N maintained for 15 s.

In vitro *bioactivity tests*

The scaffolds were immersed in 60 mL of SBF solution (8.035 g/L of NaCl, 0.355 g/L of $NaHCO_3$, 0.225 g/L of KCl, 0.231 g/L of $K_2HPO_4{\cdot}3H_2O$, 0.311 g/L of $MgCl_2{\cdot}6H_2O$ and 0.292 g/L of $CaCl_2$, pH 7.4, 37 °C) to evaluate bioactivity, with the solution renewed every two days. At 14 and 28 days, the scaffold was taken out and rinsed with ultra-pure water three times and then dried at 40 °C for 6 h. Finally, the surface morphology of the scaffold was examined using SEM after sputter-coating with gold.

Degradability tests

The scaffolds were immersed in PBS (37 °C, pH 7.4) to assay degradability. The ratio of scaffold weight to solution volume was 10 mg/mL. Weight loss at 7, 14, 21 and 28 days after immersion was calculated by recording scaffold weights before and after immersion. After immersion tests, pH was obtained with a pH meter, and Ag ion concentration was analyzed with an inductively coupled plasma-atomic emission spectrometer (ICP-AES, Baird Co., USA).

Evaluation of antibacterial activity

The bacterial inhibition zone method was adopted to investigate the antibacterial activity of scaffolds against *E. coli*. In detail, bacterial suspensions at a concentration of 1×10^6 CFU/mL were uniformly spread on a culture plate containing agar medium. The scaffolds were placed in the center of the plate and cultured for 24 h at 37 °C. After 24 h, the inhibition zones around the scaffolds were recorded using a digital camera.

Turbidimetry was used to further quantitatively analyze the antibacterial properties of the scaffolds. The scaffolds were soaked in transparent test tubes filled with bacterial suspensions (1×10^5 CFU/mL) and incubated for 24 h at 37 °C. Test tubes containing culture medium only and bacterial suspension without scaffold served as a blank group and control group, respectively. The turbidities of the test-tube suspensions were recorded by a digital camera. Absorbance at 600 nm was determined with a microplate reader (SAF-6801, BAJIU Corporation, Shanghai, China). The bacterial inhibition rate was calculated as $(B-A)/B\times100\%$, in which A and B represent the optical densities of bacterial suspensions with and without scaffolds, respectively. In addition, after culture for 1, 4 and 7 days, the bacteria on scaffolds were fixed with glutaraldehyde at 4 °C for 24 h, then washed, and dehydrated with gradient ethanol solution (25%, 50%, 75%, 90%, and 100%) for 10 min. The dried scaffolds were then observed by SEM.

In vitro *cell experiments*

Human umbilical cord mesenchymal stem cells were used for cell experiments. The cells were cultured in DMEM with 10% FBS, 1% penicillin, and streptomycin in a 24-well tissue culture plate. Before seeding cells, scaffolds were sterilized by immersing in 75% ethanol overnight and then exposing under ultraviolet light for 1 h in biological safety cabinet. The cells were seeded onto the scaffold samples (1×10^4 cells per well) and incubated in a humid environment (37 °C, 5% CO_2), with culture medium refreshed every two days. The scaffold/cell samples were harvested at 1, 4, and 7 days and fixed in 3% glutaraldehyde, then rinsed with PBS, and dehydrated in a graded ethanol series. The dehydrated scaffold/cell samples were then observed by SEM.

For a live/dead viability assay, the cells were stained using Calcein-AM and Ethidium homodimer-1 reagent for 30 min after culture for 1, 4, and 7 days. The cells were observed using a fluorescence microscope (BX60, Olympus Co., Japan).

A counting kit-8 (CCK-8) assay was also carried out. After culture for 1, 4, and 7 days, the cells on scaffolds were removed and washed with PBS. Next, 10 μL of CCK-8

reagent was added and incubated for another 4 h. Optical density was then detected using a microplate reader (Beckman, USA) at 450 nm.

Alkaline phosphatase (ALP) activity was investigated to evaluate cell differentiation ability. At 7 and 14 days, the scaffold/cell samples were washed two times with PBS and then cultured in RIPA lysis Buffer. Subsequently, total protein content and ALP activity were determined for the cells adhered on scaffolds. First, the obtained cell lysate was mixed with p-nitrophenyl phosphate solution. After incubation for 15 min, absorbance at 405 nm was determined using a microplate reader to assess the amount of p-nitrophenyl. ALP activity was obtained by normalizing the amount of p-nitrophenyl to total protein content.

In vivo *animal experiments*

Eighteen adult New Zealand rabbits were used in the animal experiments, with approval of the Xiangya Hospital Animal Experimental Ethics Committee. The experimental rabbits were divided into three groups: a PLLA scaffold group ($n=6$), a PLLA@HA@Ag scaffold group ($n=6$), and a control group without scaffold implantation ($n=6$). Before surgery, rabbits were anesthetized with an intramuscular injection of 2% sodium pentobarbital (35 mg/kg). Segmental 15-mm-long bone defect models were constructed in the midshaft of the left forearm radius. For the PLLA@HA@Ag and PLLA scaffold groups, the defect sites were implanted with scaffolds, then sutured with resorbable suture, and sterilized with iodine. The rabbits were injected with penicillin for 3 days and then fed normally.

At 4 and 8 weeks post-implantation, rabbits were sacrificed to harvest the radius specimens, which were investigated using an X-ray imaging system (IVIS Lumina XR instrument, Perkin-Elmer, USA) and micro-computed tomography (micro-CT) imaging system (SkyScan, Bruker, Belgium). Subsequently, the specimens were decalcified in disodium ethylenediaminetetraacetate dihydrate and dehydrated in a graded series of ethanol. The samples were embedded in paraffin and sectioned at a thickness of 5 μm. Tissue sections were stained with hematoxylin and eosin (H&E) and Masson's trichrome (Masson, Beijing Solarbio Science & Technology Co., Ltd., China) and observed with a slide scanner microscope (Olympus VS120-L100, Japan). The fraction of new bone area was analyzed using ImageJ software.

Statistical analysis

All tests were carried out at least three times. The obtained data were expressed as averages ± deviation. SPSS v19.0 software was used to analyze statistical significance, in which a p value less than 0.05 was recognized as statistically significant.

Results and discussion

Characterization of PLLA@HA@Ag powder

As can be seen in Fig. 1a, the PLLA@HA@Ag and original PLLA powders were observed under SEM, which exhibited irregular shapes. Their particle size distribution is shown in Fig. 1b. The average particle size of both PLLA and PLLA@HA@Ag powder was about 100 μm.

The phase composition of the PLLA@HA@Ag and PLLA powders was investigated using XRD, with results presented in Fig. 1c. As a semi-crystalline polymer, PLLA exhibited the typical broad characteristic peak located at 16.2°. By comparison, several new diffraction peaks were observed in the PLLA@HA@Ag powder. Specifically, the four new diffraction peaks located at 38.13° (111), 44.35° (200), 64.52° (220), and 77.44° (311) corresponded to metallic Ag (JCPDS card number 04-0783), whereas another four new diffraction peaks located at 25.9° (002), 32.10° (211), 46.76° (213), and 54.91° (004) corresponded to HA (JCPDS card number 09-0432).

XPS analysis was also carried out to further characterize the composition of PLLA@HA@Ag powder, with the overall spectrum depicted in Fig. 1d. In general, O, N, Ag, Ca, P, and C elements were detected from PLLA@HA@Ag powder. Furthermore, the N1s core level spectrum revealed the presence of –N–H (Fig. 1e), which should be derived from coated PDA on PLLA. As shown in Fig. 1f, the peaks located at 368.3 and 374.3 eV correspond to the binding energy of $Ag_{3d3/2}$ and $Ag_{3d5/2}$, respectively, which indicated the presence of Ag nanoparticles in PLLA@HA@Ag powder. The peaks located at 351.0 and 347.5 eV correspond to the binding energy of $Ca_{2p1/2}$ and $Ca_{2p3/2}$ (Fig. 1g), and the peaks located at 133.0 eV correspond to the binding energy of $P_{2p3/2}$ (Fig. 1h), which confirmed the formation of HA nanoparticles.

The TEM images of PLLA@HA@Ag powder are shown in Fig. 2. It can be seen that a layer of translucent material with a thickness of 5–7 nm, recognized as PDA, covered the PLLA surface. Specifically, a few spherical

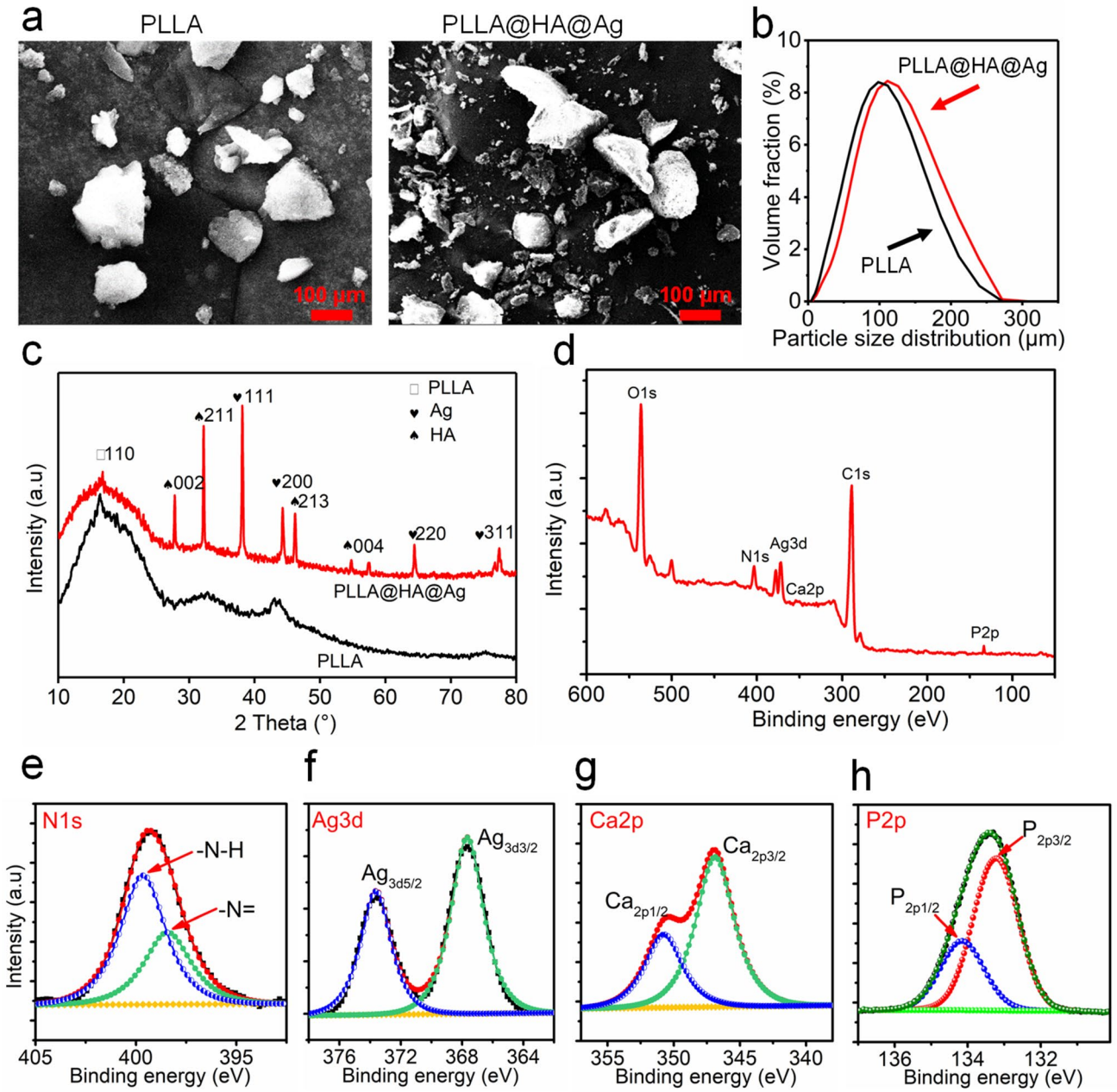

Fig. 1 Characterization of PLLA@HA@Ag and PLLA powders: **a** SEM images; **b** the corresponding particle size distribution; **c** XRD results; **d** the overall XPS spectrum obtained from PLLA@HA@Ag powder and detailed spectrum of N1s (**e**), Ag3d (**f**), Ca2p (**g**), and P2p (**h**)

nanoparticles were embedded in the PDA layer. The crystalline inter-planar spacing determined from the nanoparticles decorated on PLLA surface was 0.275 and 0.233 nm, which was assigned to HA and metallic Ag, respectively [32].

Combining the above XRD, XPS, and TEM analysis, it is reasonable to conclude that HA and Ag nanoparticles successfully grew in situ on PLLA powder. The corresponding mechanism is schematically depicted in Fig. 3. It is well accepted that the mussel-inspired material DA, with abundant catechol and amine groups, is able to adhere onto almost every kind of substrate [33]. In the present study, DA tightly adhered to PLLA powder and then self-polymerized into PDA in a weak alkaline environment, which created a large number of active sites for subsequent in situ growth of HA and Ag nanoparticles. In detail, the catechol groups absorbed Ca^{2+} in SBF by chelation, and subsequently absorbed HPO_4^{2-} through electrostatic interaction, thus achieving nucleation of HA [34]. Lastly, in $AgNO_3$ solution, Ag^+ was reduced into Ag nanoparticles

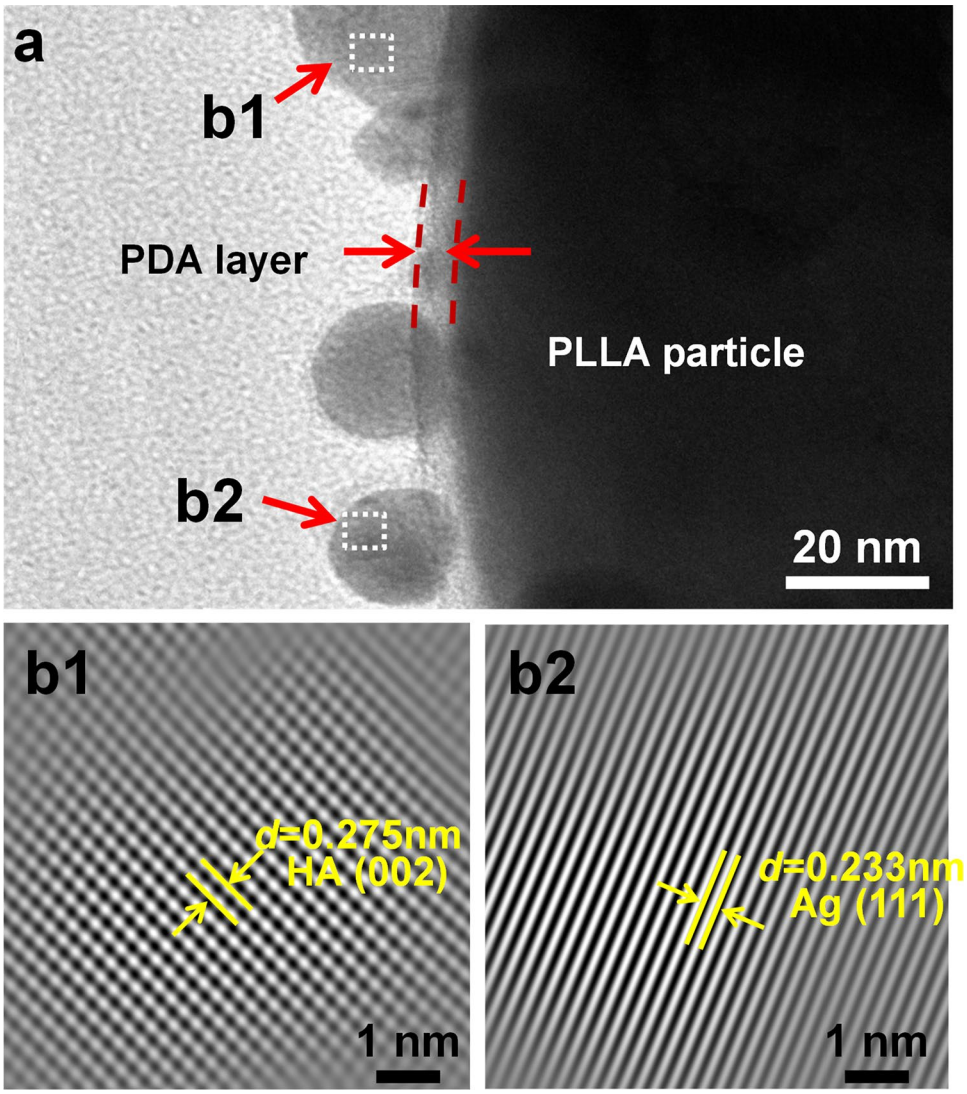

Fig. 2 TEM image of PLLA@HA@Ag powder (**a**), and high-resolution TEM images of HA (**b1**) and Ag (**b2**) nanoparticles

due to the weak reducibility of reserved catechol groups. It should be noted that ion concentration and immersion time significantly affected the deposition rate of HA and Ag nanoparticles [35]. Our experiments revealed that reduced immersion time limited the amount of HA. In the control group, an extended immersion period resulted in excessive HA, which occupied the growth space for Ag nanoparticles. In fact, some researchers have successfully obtained in situ generation of HA and Ag nanoparticles on PDA by adjusting the immersion period [36].

Physicochemical properties of scaffolds

The PLLA@HA@Ag powder was developed into porous scaffolds by SLS, which presented a porous structure, as shown in Fig. 4a. An ideal bone scaffold requires a porous structure for cell growth and reproduction [37, 38].

Low-magnification SEM observation revealed that a large amount of partially melted powder is attached on the struts, resulting in a rather rough scaffold surface pores and ravines (Fig. 4b). In fact, a certain amount of surrounding powder tended to approach the molten pool during laser sintering, thus leading to formation of bonded powder particles without risk of detachment [39]. A rough surface is believed capable of providing various mechanical stimuli for adhered cells and promoting their growth and differentiation. High-magnification SEM observation revealed that numerous particles with sizes ranging from 10 to 100 nm (marked by red arrows in Fig. 4b) were homogeneously distributed in the matrix of the PLLA@HA@Ag scaffold. The corresponding EDS spectrum confirmed that these particles are HA (P1, Fig. 4b) or Ag nanoparticles (P2, Fig. 4b). Clearly, the in situ growth technique yielded nano-size particles, rather than micro-size particles. In general, nano-size particles possess several advantages over micro-size articles. For instance,

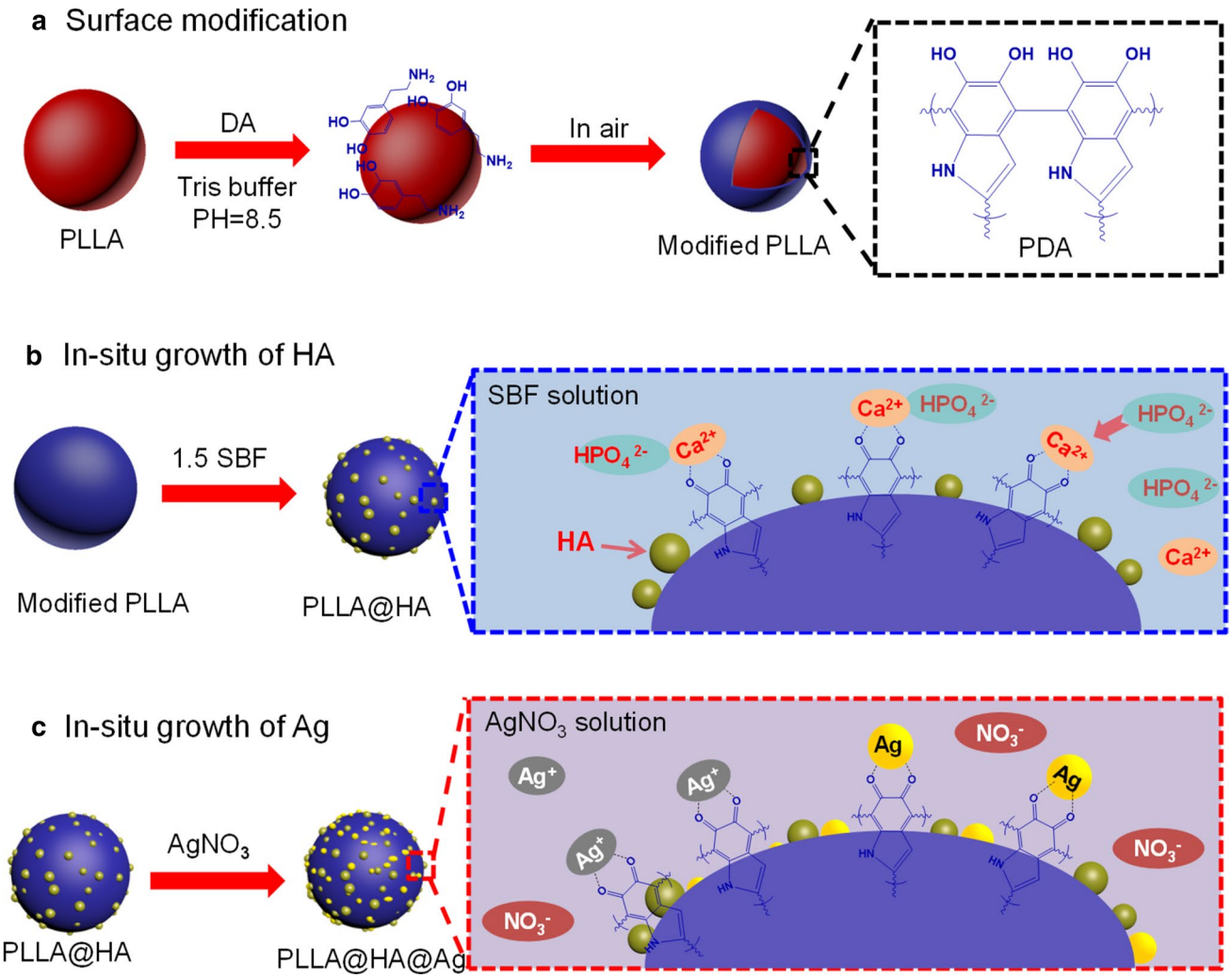

Fig. 3 Mechanism for in situ growth of HA and Ag nanoparticles on PLLA: **a** DA adhered on PLLA powder and self-polymerized into PDA in a weak alkaline environment; **b** HA grown in situ on PDA-modified PLLA powder by chelation and electrostatic interaction in 1.5 × SBF solution; **c** Ag^+ was reduced into Ag nanoparticles on PLLA@HA powder in $AgNO_3$ solution

Ag nanoparticles can produce a stronger antibacterial effect than micro-size ones, due to their greater surface area [40, 41]. The in situ growth technique also solves the aggregation problem of incorporated nanoparticles, which is of great importance in composite scaffolds. An irrefutable fact is that homogeneously distributed nanoparticles in polymer matrix would greatly improve the mechanical properties of the scaffold.

The mechanical performance of as-built scaffolds was evaluated by compression tests, with representative stress–strain curves depicted in Fig. 4c. Specifically, the obtained curves begin with a parabola going upward, due to uneven contact between samples and pressure head. The curves then experience a linear increase in stress with strain, and a subsequent fracture region with sharply decreasing stress. The calculated ultimate strength is shown in Fig. 4d. The PLLA@HA@Ag scaffold exhibited an enhanced ultimate strength of 13.1 MPa, which can be attributed to the particle reinforcement effect caused by the HA and Ag nanoparticles. The PLLA@HA@Ag scaffold also possessed a greater hardness (23.5 Hv) than the PLLA scaffold.

The hydrophilicity of PLLA@HA@Ag and PLLA scaffolds was investigated by measurement of water contact angles, as seen in Fig. 4e. The PLLA scaffold exhibited a relatively large contact angle of 95.1° ± 2.2°, consistent with its poor hydrophilicity as reported by previous investigators [42]. For the PLLA@HA@Ag scaffold, the water contact angle was decreased to 77.6° ± 3.4°. Apparently, the introduced HA and PDA with good hydrophilicity altered the surface texture and chemical composition of the scaffold, thus improving surface hydrophilicity. In general, scaffolds with enhanced hydrophilicity favor exchange of nutrients and ingrowth of bone tissue.

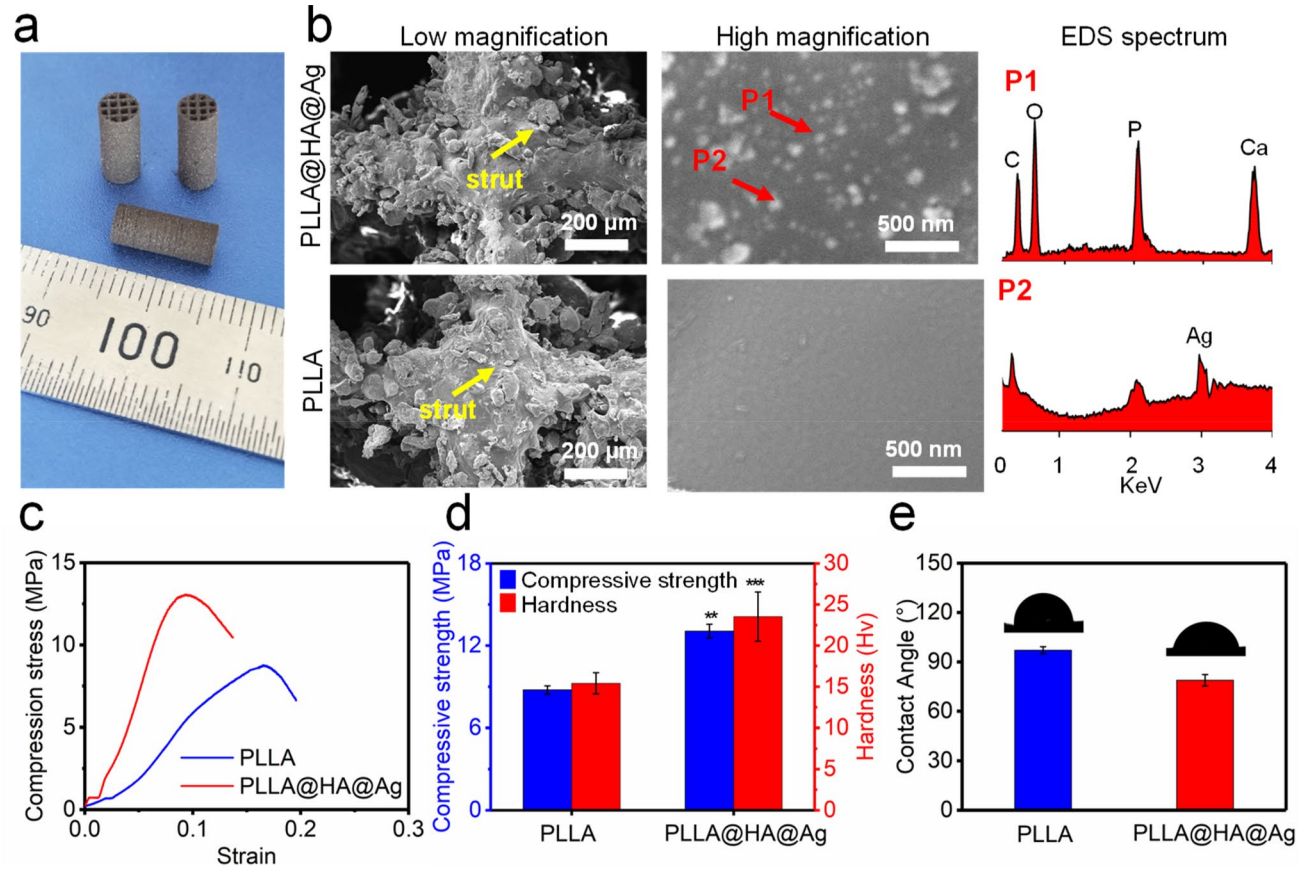

Fig. 4 The characterization of as-built PLLA@HA@Ag and PLLA scaffolds: **a** General view of PLLA@HA@Ag scaffolds; **b** SEM combined with EDS analysis, showing the microstructural features of scaffolds (red arrows mark HA (P1) and Ag (P2) nanoparticles, which were analyzed by EDS); **c** compressive stress–strain curves; **d** ultimate compressive strength and hardness; **e** surface contact angles of the scaffolds. $n=3$, $^{**}p<0.01$, $^{***}p<0.001$

Mineralization and degradation behavior

It is well accepted that mineralization ability, including specifically apatite-forming ability, is vital for the ability of a scaffold to provide a favorable bonding interface with new bone tissue [43]. Therefore, we investigated the mineralization ability of scaffolds using SBF immersion tests, with the scaffold surface shown in Fig. 5a. A large number of spherical particles deposited on the PLLA@HA@Ag scaffold and increased considerably with extension of the immersion period from 14 to 28 days. These particles consisted mainly of Ca, P, C and O, with a Ca/P ratio of about 1.61 (Fig. 5b). Thus, it is reasonable to deduce that the apatite was deposited on the PLLA@HA@Ag scaffold. In comparison, only a few small-sized pores were observed on the PLLA scaffold, in line with its rather poor mineralization ability. These results confirmed that the HA grown in situ endowed the scaffold with excellent bioactivity.

Bone scaffolds also require good biodegradability, in order to fully serve their function as temporary substitutes. In the present study, the degradation rate of scaffolds was assessed by detecting weight loss during PBS immersion tests, with results shown in Fig. 5c. The PLLA scaffold suffered a mass loss of 6.3% after a 28-day immersion. In comparison, the PLLA@HA@Ag scaffold exhibited a slightly reduced mass loss of 5.1%. It was believed that the incorporated HA prompted the deposition of Ca-P layer, which in turn delayed the degradation of PLLA matrix, despite the improvement of hydrophilicity.

The pH variation of the PBS solution immersed with the scaffolds was also monitored, with results shown in Fig. 5d. In the PLLA scaffold, the pH gradually dropped to 6.9, reflecting the generation of acid by-products that were formed as PLLA degraded. In the PLLA@HA@Ag scaffold, the pH was higher than that of PLLA scaffold, decreasing to 7.1 after 28 days. Because the PLLA@HA@Ag scaffold leaches HA nanoparticles during degradation, the leached

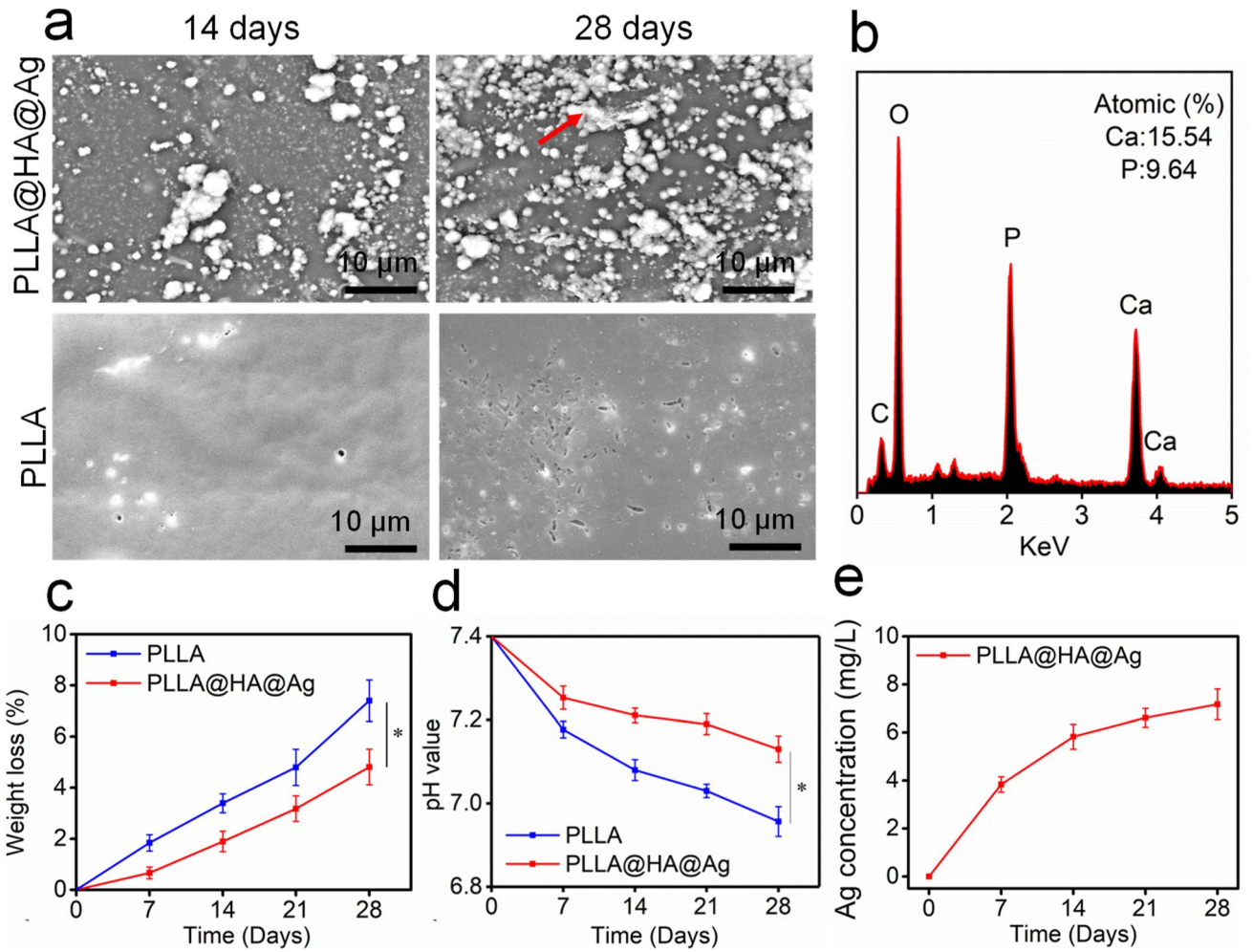

Fig. 5 Mineralization and degradation behavior of PLLA@HA@Ag and PLLA scaffolds: **a** surface morphology after immersion in SBF for 14 and 28 days; **b** EDS analysis of the marked area (marked by arrows) in Fig. 4a; **c** weight loss of scaffolds during PBS immersion; **d** variation in pH; **e** Ag concentration of the immersed PBS solution. $n=3$, $^{*}p<0.05$

HA was able to neutralize the acid products created by degradation of PLLA [44], thus increasing pH to some extent. Ag ion concentration released from PLLA@HA@Ag scaffold is shown in Fig. 5e. It was found that the released Ag ion gradually increased to 7.1 mg/L with a 28-day immersion period.

Antibacterial efficacy

Strong and effective antibacterial ability is of great significance for bone implants. In the present study, in situ grown Ag was expected to introduce desirable antibacterial properties to the scaffolds. To test this hypothesis, the antibacterial properties of scaffolds were investigated using inhibition ring tests. Culture plates containing scaffolds and *E. coli* were photographed after one day of culture, as shown in Fig. 6a. No obvious bacterial inhibition zone was observed for the PLLA scaffold. In comparison, an obvious bacterial inhibition zone with an enlarged diameter appeared around the PLLA@HA@Ag scaffold, indicating its strong antibacterial activity.

Turbidity analysis tests were also conducted, as shown in Fig. 6b. It can be seen that the turbidity of cultures incubated with PLLA scaffold is similar to that of the control group, indicating that the PLLA scaffold exerted no inhibition effect on bacterial growth. Significantly, the culture medium incubated with PLLA@HA@Ag scaffold became transparent, indicating that the bacterial growth was strongly inhibited. The corresponding bacterial inhibition rates are shown in Fig. 6c. The PLLA@HA@Ag scaffold exhibited an inhibition rate of over 92.5%, whereas the PLLA scaffold showed almost no antibacterial activity.

The bacterial colonies cultured on scaffolds for varied periods are shown in Fig. 6d. As is evident in Fig. 6d, a large number of rod-like bacteria adhered to the PLLA scaffold. The bacteria increased considerably in number with

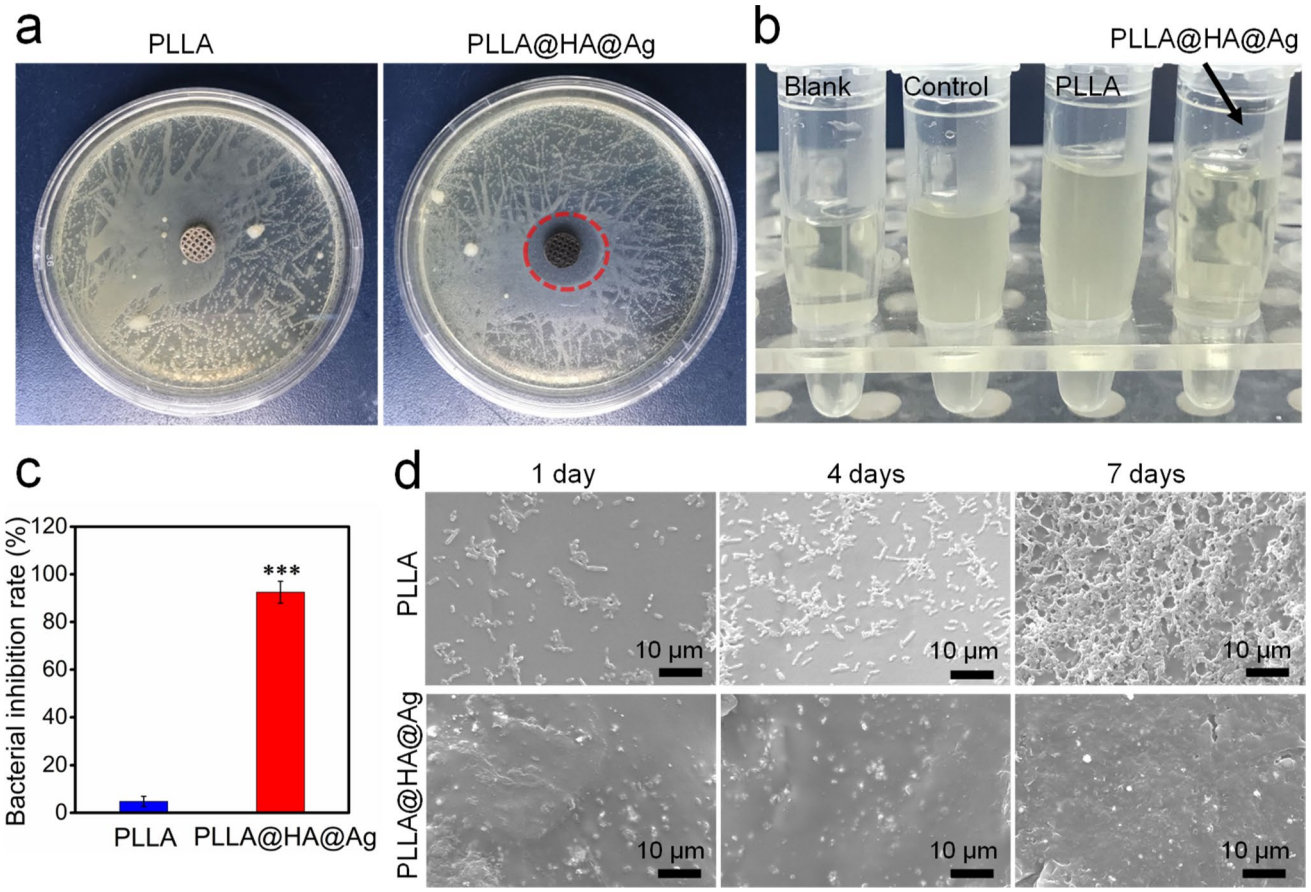

Fig. 6 The antibacterial activities of PLLA@HA@Ag and PLLA scaffolds: **a** inhibition rings around the scaffolds; **b** turbidity of the culture medium incubated with scaffolds for 24 h; **c** bacterial inhibition rate; **d** SEM observation of the bacterial cultured on scaffolds for 1, 4, and 7 days. $n = 3$, $^{***}p < 0.001$

increased culture time, covering the scaffold almost completely scaffold after 7 days in culture. In contrast, only a few *E. coli* colonies could be found on the PLLA@HA@Ag scaffold. These results further confirm that the PLLA@HA@Ag scaffold possesses a strong ability to inhibit bacterial survival and adhesion.

Our results demonstrate that the PLLA@HA@Ag scaffold shows strong antibacterial activity, which can be ascribed to incorporation of in situ grown Ag nanoparticles. As shown by the immersion tests, Ag ion leached from PLLA@HA@Ag scaffold by degradation and diffusion into the physiological consideration. It is of significant relevance that leached Ag ion binds to bacterial membranes with negative charge via electrostatic effects, and interacts with thiol groups on membrane proteins [45, 46], thereby altering membrane permeability and disrupting membrane integrity [47]. In addition, with their high catalytic ability and reduction potential, Ag ions can catalyze the single-electron reduction of O_2 and damage the bacterial respiratory chain, thus generating oxidizing reactive oxygen species (ROS) [48]. ROS activity is known to destroy the molecular structure of DNA by substituting hydrogen bonds, thus inhibiting replication of bacterial mRNA [49, 50]. All of these actions generate a strong antibacterial effect by damaging bacterial reproduction and survival.

In vitro *cell response*

An ideal scaffold should provide a favorable micro-environment for cell adhesion, and proliferation [51, 52]. Stem cells can be induced in vitro to generate human cells of various tissue types, a capability useful for the establishment of human cell/tissue models and the development of new bone implants. For this reason, stem cells were used in our cell experiments. Stem cells incubated on PLLA@HA@Ag and PLLA scaffolds for 1, 4, and 7 days are shown in Fig. 7a. Green represents live cells, while red represents dead cells. In general, most cells on the scaffolds exhibited good morphology, despite the presence of a few dead cells, especially for PLLA scaffold. In particular, more cells with larger numbers of filopodia were observed in the PLLA@HA@Ag scaffold at day 4 and 7.

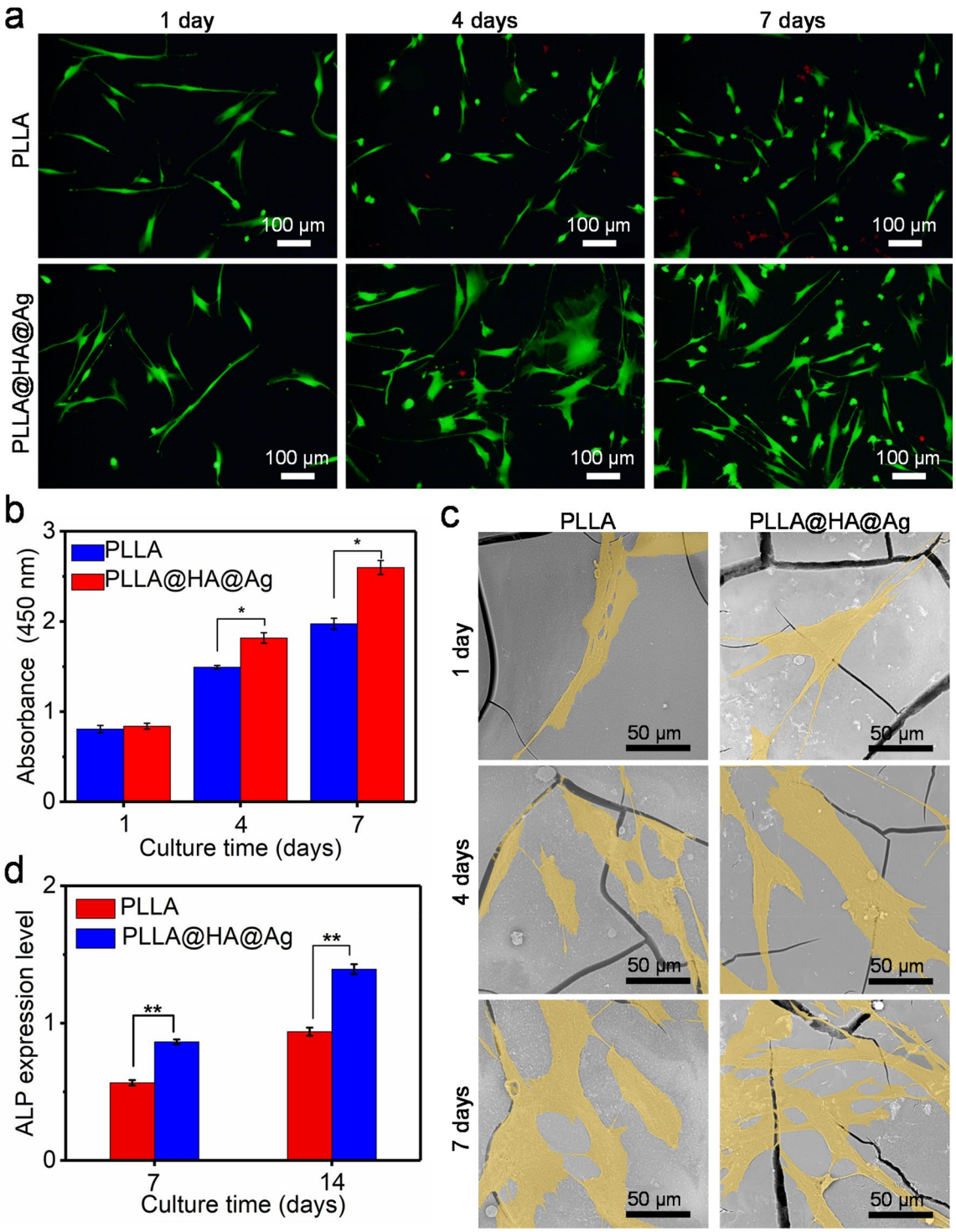

Fig. 7 Stained stem cells after 1, 4, and 7 days of culture (**a**), optical density from CCK-8 assays (**b**), SEM images of adhered stem cells on scaffolds after 1, 4, and 7 days of culture (cells are labeled yellow for easy identification) (**c**), and ALP expression levels (**d**). $n=3$, $^{*}p<0.05$, $^{**}p<0.01$

The viability of stem cells cultured on scaffolds was quantitatively investigated using a CCK-8 assay, as shown in Fig. 7b. For PLLA scaffolds, the optical density, which is positively correlated with cell number, was 0.81 at day 1, 1.49 at day 4, and 1.97 at day 7. For the PLLA@HA@Ag scaffold, the optical density was 0.83 at day 1, 1.82 at day 4, and 2.60 at day 7. These results further confirmed

that PLLA@HA@Ag scaffold promoted stem cell growth more effectively than the PLLA scaffold.

Stem cell adhesion behavior on scaffolds was investigated by SEM, as shown in Fig. 7c. SEM images show several cracks on the matrix surface, which might be attributed to dehydration before SEM observation. All stem cells adhered tightly to the scaffolds and exhibited flat, stretched morphologies with large numbers of filopodia. Notably, more stem cells attached to PLLA@HA@Ag scaffold and exhibited abundant filopodia, indicating that the PLLA@HA@Ag scaffold promoted cell attachment.

ALP expression of stem cells incubated on PLLA@HA@Ag and PLLA scaffolds was also assessed (Fig. 7d). As an early osteoblastic differentiation marker, ALP expression increased as culture time increased from 7 to 14 days. Specifically, ALP levels of cells on the PLLA@HA@Ag scaffold were markedly higher than in cells on the PLLA scaffold.

In the present study, in vitro cell tests indicate that cells on the PLLA@HA@Ag scaffold showed improved cell behavior, including cell attachment, proliferation, and differentiation. We hypothesize that the changed surface

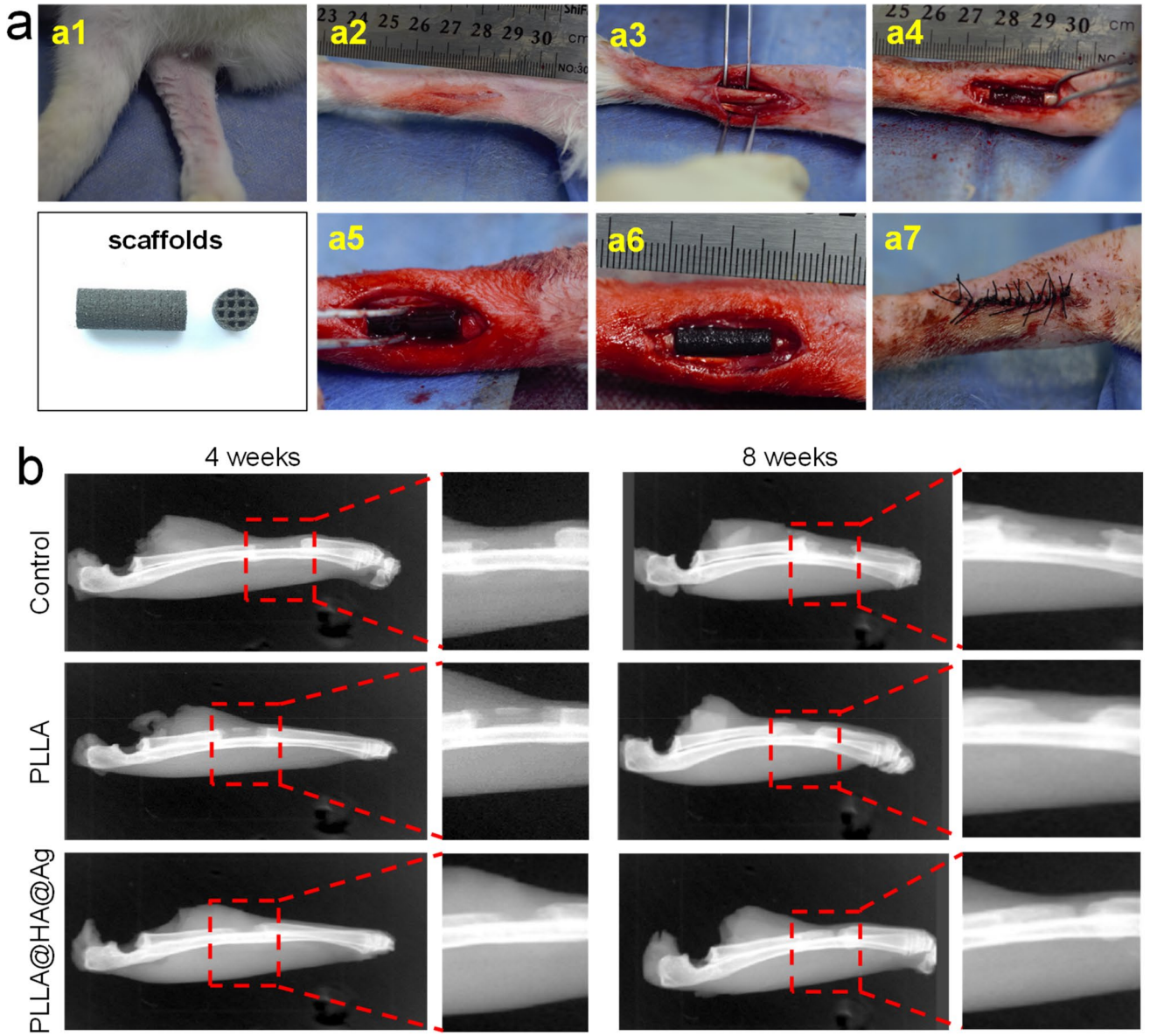

Fig. 8 **a** Protocol for construction of the complete segmental bone defect model and scaffolds implantation: (a1) rabbit leg after shaving; (a2) disinfection with tincture of iodine; (a3) exposed radius after a longitudinal incision; (a4) complete segmental bone defect model; (a5, a6) scaffold implantation at the defect site; (a7) suturing bone defect. **b** Representative X-ray images of bone defect site at 4 and 8 weeks post-operation

texture and improved hydrophilicity should account for the increased cell attachment and proliferation seen on these scaffolds. In addition, HA has good biocompatibility and bioactivity, which might also increase cell proliferation. HA bioactivity might also explain the increased osteogenic differentiation of cells on the PLLA@HA@Ag scaffold [53].

In vivo *bone regeneration*

A complete segmental bone defect and partial segmental bone defect are the two common bone defect models that have used in animal experiments [54, 55]. In the present study, a complete segmental bone defect model was adopted (Fig. 8a), because it more accurately represented the osteogenesis ability of bone tissue engineering scaffolds than the partial segmental bone defect model. Laser-sintered PLLA@HA@Ag and PLLA scaffolds were implanted into radius-bone defects of New Zealand rabbits, with an untreated bone defect model as control. The clinical process including model construction and scaffold implantation was smooth-going within 30 min. After the operation, all the rabbits showed no obvious discomfort.

X-ray images of rabbit radius at 4 and 8 weeks post-operation are shown in Fig. 8b. The control group showed no obvious new bone formation at 4 weeks, and very little bone tissue at 8 weeks, confirming that the segmental bone defect lacked self-repair ability. In the PLLA scaffold group, clear callus formation was observed at the edge between the implanted scaffold and surrounding bone tissue at 4 weeks post-operation. At 8 weeks, more callus formed despite the fact that partial bone defects still remained, suggesting that the microenvironment constructed by the PLLA scaffold facilitated new bone formation to some extent. Enhanced formation of new bone formation, with favorable interface to scaffold was observed in the PLLA@HA@Ag scaffold group compared to the PLLA scaffold. These observations indicated favorable osteoconduction ability in the PLLA@HA@Ag scaffold.

Bone regeneration ability was also assessed by micro-CT, as shown in Fig. 9a. Three-dimensional (3D) reconstructed images show that good repair of the bone defect region repaired well in the PLLA@HA@Ag scaffold group at 8 weeks. The corresponding quantitative analysis revealed that the PLLA@HA@Ag scaffold group exhibited significantly enhanced bone mineral densities (BMD) at 4 and 8 weeks, compared to those of the PLLA scaffold group (Fig. 9b). Similarly, the PLLA@HA@Ag scaffold group exhibited higher BV/TV ratios at 4 weeks (55.7%) and 8 weeks (76.9%) than the PLLA scaffold group (36.3% at 4 weeks and 61.4% at 8 weeks) (Fig. 9c). In addition, no obvious bone-defect repair was detected in the control group.

Histologic analysis was performed to investigate the dynamics of bone formation, with Masson and H&E staining of longitudinal sections shown in Fig. 10a and 10b, respectively. In general, both PLLA@HA@Ag and PLLA scaffolds presented good in vivo biocompatibility without obvious inflammation. Specifically, a small amount of new bone, combined with loose fibrous tissue and blood vessels, was observed at 4 weeks post-operation, confirming that the implanted scaffold successfully induced ingrowth of new bone and blood vessels. At 8 weeks, new bone increased considerably, with a large amount of visible mature bone lamellae, whereas fibrous tissue decreased in both PLLA@HA@Ag and PLLA scaffolds. In addition, scaffold area decreased with only a few remain in small-sized cavities due to natural degradation characteristics of the scaffold. Scaffold degradation characteristics are of great significance to bone tissue engineering. At the initial stages, the scaffold mainly plays the role of mechanical support. Subsequently, the scaffold degrades and is gradually replaced by new bone. Quantitative determination of the fraction of newly formed bone is shown in Fig. 10c. The relative area of newly formed bone gradually increased after implantation. Specifically, the relative area of newly formed bone in the PLLA@HA@Ag scaffold group was $71.8\% \pm 2.2\%$ at 8 weeks, considerably greater than that in the PLLA scaffold group ($49.2\% \pm 1.6\%$).

In this study, PLLA@HA@Ag scaffold promoted bone generation in vivo more effectively than PLLA scaffold, as shown by X-ray, micro-CT, and histological analysis. The improved bone generation can be ascribed to the enhanced adhesion and proliferation of bone-related cells with the PLLA@HA@Ag scaffold. This hypothesis is supported by the fact that the incorporated HA nanoparticles are the main inorganic component of natural bone and possess excellent osteogenic activity. Previous researchers reported that the surface topography of HA is able to change cytoskeleton tension, resulting in promotion of the Yes-associated protein (YAP) and PDZ-binding motif (TAZ) signaling pathway, which in turn increases cell attachment and growth [53]. It has also been shown that HA promotes the adhesion, proliferation, and osteogenic differentiation of bone marrow stromal cells through activation of the extracellular signal-related kinases (ERK) and p38 mitogen-activated protein kinase (MAPK) signaling pathways [56]. It is also possible that HA particles released from the scaffolds during degradation could be incorporated into lysosome via endocytosis, leading to release of PO_4^{3-} in the acidic lysosomal environment and activation of the adenosine-triphosphate (ATP)-induced cAMP/PKA pathway because of the ATP generated by interaction between PO_4^{3-} and adenosine diphosphate (ADP), ultimately promoting osteogenesis [57]. In summary, the PLLA@HA@Ag scaffold enhances osteogenesis, showing great potential as a useful clinical tool for segmental bone repair.

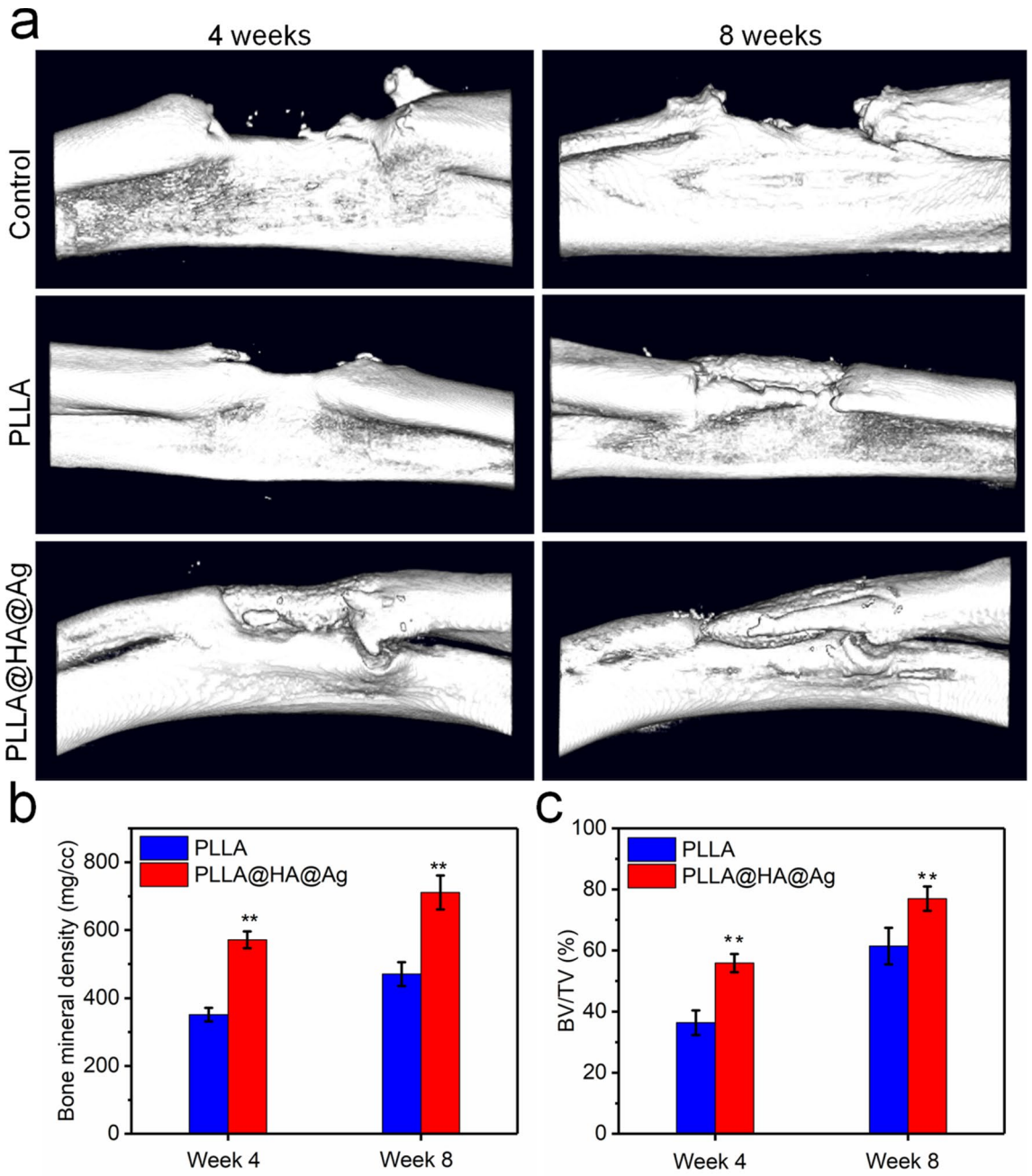

Fig. 9 Representative 3D images showing the bone defect region at 4 and 8 weeks post-operation (**a**), and bone mineral density (**b**) and BV/TV ratio (**c**) derived from micro-CT data. $n = 3$, $^{**}p < 0.01$

Conclusions

In this study, an in situ generation technique was used to grow HA and Ag nanoparticles on PLLA powder, which was developed into a composite bone scaffold using SLS. Results demonstrated that HA and Ag nanoparticles were homogenously distributed in the resulting scaffold matrix. SBF immersion tests indicated that the scaffold possesses excellent bioactivity in forming an apatite layer on the scaffold in physiological conditions. This scaffold also exhibits strong antibacterial activity. In vitro cell experiments revealed that the scaffold showed improved cell behavior, including cell attachment, proliferation, and differentiation. In vivo tests confirmed that the scaffold significantly promoted bone generation with a relative area of 71.8% new bone at 8 weeks after implantation. All of these promising findings suggest that the combined osteogenesis and antibacterial activity of this bifunctional scaffold has great potential for clinical applications to bone repair.

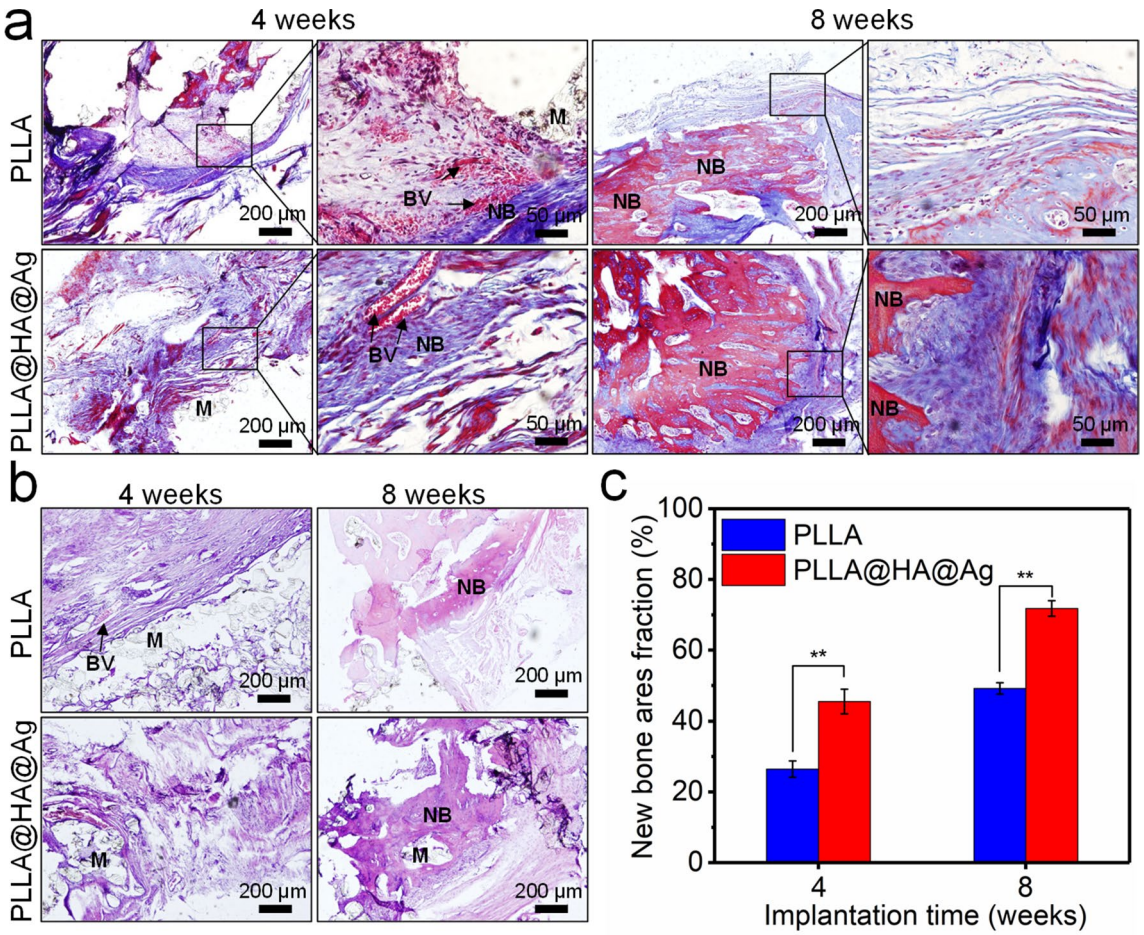

Fig. 10 Representative histological sections stained by Masson (**a**) and H&E (**b**) staining at bone-defect sites 4 and 8 weeks post-surgery (M represents scaffold materials; NB represents new bone; BV represents blood vessels), and the calculated new bone fraction (**c**). $n=3$, $^{**}p<0.01$

Acknowledgements This study was supported by the following funds: (1) National Natural Science Foundation of China (Nos. 51935014, 82072084, and 81871498); (2) Jiangxi Provincial Natural Science Foundation of China (Nos. 20192ACB20005 and 2020ACB214004); (3) The Provincial Key R & D Projects of Jiangxi (No. 20201BBE51012); (4) Guangdong Province Higher Vocational Colleges & Schools Pearl River Scholar Funded Scheme (2018); (5) Shenzhen Science and Technology Plan Project (No. JCYJ20170817112445033); (6) Innovation Team Project on University of Guangdong Province (No. 2018GKCXTD001); (7) Technology Innovation Platform Project of Shenzhen Institute of Information Technology 2020 (No. PT2020E002); (8) Open Research Fund of Jiangsu Key Laboratory of Precision and Micro-Manufacturing Technology; (9) China Postdoctoral Science Foundation (No. 2020M682114).

Author contributions YWY and YC were involved in conceptualization, investigation, writing—original draft; FD and LDS were involved in visualization and resources; ZYZ and SPP helped in writing—review & editing; and CJS contributed to supervision.

Declarations

Conflict of interest The authors declare that they have no conflict of interest.

Ethical approval The animal experiments in this work have obtained the permission from Xiangya Hospital Animal Experimental Ethics Committee.

References

1. Oladapo BI, Zahedi SA, Ismail SO et al (2021) 3D printing of PEEK/HAp scaffold for medical bone implant. Bio-des Manuf 4:44–59. https://doi.org/10.1007/s42242-020-00098-0
2. Liu H, Lin M, Liu X et al (2020) Doping bioactive elements into a collagen scaffold based on synchronous self-assembly/mineralization for bone tissue engineering. Bioact Mater 5(4):844–858. https://doi.org/10.1016/j.bioactmat.2020.06.005
3. Reiter T, Panick T, Schuhladen K et al (2019) Bioactive glass based scaffolds coated with gelatin for the sustained release of icariin. Bioact Mater 4:1–7. https://doi.org/10.1016/j.bioactmat.2018.10.001
4. Bigham A, Foroughi F, Ghomi ER et al (2020) The journey of multifunctional bone scaffolds fabricated from traditional toward modern techniques. Bio-des Manuf 3:281–306. https://doi.org/10.1007/s42242-020-00094-4

5. Didekhani R, Sohrabi MR, Seyedjafari E et al (2018) Electrospun composite PLLA/Oyster shell scaffold enhances proliferation and osteogenic differentiation of stem cells. Biologicals 54:33–38. https://doi.org/10.1016/j.biologicals.2018.04.006
6. Poh PS, Hutmacher DW, Holzapfel BM et al (2016) In vitro and in vivo bone formation potential of surface calcium phosphate-coated polycaprolactone and polycaprolactone/bioactive glass composite scaffolds. Acta Biomater 30:319–333. https://doi.org/10.1016/j.actbio.2015.11.012
7. de Siqueira L, Ribeiro N, Paredes M et al (2019) Influence of PLLA/PCL/HA scaffold fiber orientation on mechanical properties and osteoblast behavior. Materials 12(23):3879. https://doi.org/10.3390/ma12233879
8. Skadiņš I, Kroiča J, Salma I et al (2019) Influence of antibiotic-impregnated biomaterials on inflammatory cytokines. Proc Latvian Acad Sci Sect B Nat Exact Appl Sci 73(2):177–184. https://doi.org/10.2478/prolas-2019-0028
9. Zheng K, Wu J, Li W et al (2018) Incorporation of Cu-containing bioactive glass nanoparticles in gelatin-coated scaffolds enhances bioactivity and osteogenic activity. ACS Biomater Sci Eng 4(5):1546–1557. https://doi.org/10.1021/acsbiomaterials.8b00051
10. Poorraeisi M, Afshar A (2019) Synthesizing and comparing HA–TiO_2 and HA–ZrO_2 nanocomposite coatings on 316 stainless steel. SN Appl Sci 1(2):155. https://doi.org/10.1007/s42452-019-0168-2
11. Khan ME, Han TH, Khan MM et al (2018) Environmentally sustainable fabrication of Ag@ g-C_3N_4 nanostructures and their multifunctional efficacy as antibacterial agents and photocatalysts. ACS Appl Nano Mater 1(6):2912–2922. https://doi.org/10.1021/acsanm.8b00548
12. Wang Y, Yan L, Cheng R et al (2018) Multifunctional HA/Cu nano-coatings on titanium using PPy coordination and doping via pulse electrochemical polymerization. Biomater Sci 6(3):575–585. https://doi.org/10.1039/C7BM01104K
13. Tian G, Zhu G, Xu S et al (2019) A novel shape memory poly (ε-caprolactone)/hydroxyapatite nanoparticle networks for potential biomedical applications. J Solid State Chem 272:78–86. https://doi.org/10.1016/j.jssc.2019.01.029
14. Hong W, Guo F, Chen J et al (2018) Bioactive glass–chitosan composite coatings on PEEK: effects of surface wettability and roughness on the interfacial fracture resistance and in vitro cell response. Appl Surf Sci 440:514–523. https://doi.org/10.1016/j.apsusc.2018.01.183
15. Mohamed MS, Kumar DS (2016) Methods of using nanoparticles, plant nanotechnology, Springer, Cham, pp 65–93. https://doi.org/10.1007/978-3-319-42154-4
16. Mallakpour S, Nouruzi N (2016) Effect of modified ZnO nanoparticles with biosafe molecule on the morphology and physiochemical properties of novel polycaprolactone nanocomposites. Polymer 89:94–101. https://doi.org/10.1016/j.polymer.2016.02.038
17. Nayak GC, Das CK (2016) LCP based polymer blend nanocomposites. Liq Cryst Polym 2016:251–272. https://doi.org/10.1007/978-3-319-22894-5
18. Zhu Y, Shen J, Zhou K et al (2010) Multifunctional magnetic composite microspheres with in situ growth Au nanoparticles: a highly efficient catalyst system. J Phys Chem C 115(5):1614–1619. https://doi.org/10.1021/jp109276q
19. Zhang X, Liu Z, Zhang X et al (2018) High-adhesive superhydrophobic litchi-like coatings fabricated by in-situ growth of nano-silica on polyethersulfone surface. Chem Eng J 343:699–707. https://doi.org/10.1016/j.cej.2018.03.012
20. Lee YH, Hsu YT, Yeh PS et al (2019) Embossed hybrid synthesis of ZnO nanocrystals on self-organized one-dimensional poly (3-butylthiophene) nanowires. Physica Status Solidi(a) 216(9):1801001. https://doi.org/10.1002/pssa.201801001
21. Yang Y, Huang Q, Payne GF et al (2019) A highly conductive, pliable and foldable Cu/cellulose paper electrode enabled by controlled deposition of copper nanoparticles. Nanoscale 11(2):725–732. https://doi.org/10.1039/C8NR07123C
22. Tang W, Ma T, Zhou L et al (2019) Polyamine-induced tannic acid co-deposition on magnetic nanoparticles for enzyme immobilization and efficient biodiesel production catalysed by an immobilized enzyme under an alternating magnetic field. Catal Sci Technol 9(21):6015–6026. https://doi.org/10.1039/C9CY01350D
23. Xie Y, Yue L, Zheng Y et al (2019) The antibacterial stability of poly (dopamine) in-situ reduction and chelation nano-Ag based on bacterial cellulose network template. Appl Surf Sci 491:383–394. https://doi.org/10.1016/j.apsusc.2019.06.096
24. JináLee S, MináSeok J, HeeáLee J et al (2018) In situ gold nanoparticle growth on polydopamine-coated 3D-printed scaffolds improves osteogenic differentiation for bone tissue engineering applications: in vitro and in vivo studies. Nanoscale 10(33):15447–15453. https://doi.org/10.1039/C8NR04037K
25. Bian SW, Liu S, Chang L (2016) Synthesis of magnetically recyclable Fe_3O_4@ polydopamine–Pt composites and their application in hydrogenation reactions. J Mater Sci 51(7):3643–3649. https://doi.org/10.1007/s10853-015-9688-3
26. Yang Y, Cheng Y, Peng S et al (2021) Microstructure evolution and texture tailoring of reduced graphene oxide reinforced Zn scaffold. Bioact Mater 6(5):1230–1241. https://doi.org/10.1016/j.bioactmat.2020.10.017
27. Shuai C, Li S, Yang W et al (2020) MnO_2 catalysis of oxygen reduction to accelerate the degradation of Fe–C composites for biomedical applications. Corros Sci 170:108679. https://doi.org/10.1016/j.corsci.2020.108679
28. Gao C, Li S, Liu L et al (2020) Dual alloying improves the corrosion resistance of biodegradable Mg alloys prepared by selective laser melting. J Magn Alloys 9(1):305–316. https://doi.org/10.1016/j.jma.2020.03.016
29. Li M, Chen AN, Lin X et al (2019) Lightweight mullite ceramics with controlled porosity and enhanced properties prepared by SLS using mechanical mixed FAHSs/polyamide12 composites. Ceram Int 45(16):20803–20809. https://doi.org/10.1016/j.ceramint.2019.07.067
30. Wang G, Qian G, Zan J et al (2020) A co-dispersion nanosystem of graphene oxide @silicon-doped hydroxyapatite to improve scaffold properties. Mater Des 199:109399. https://doi.org/10.1016/j.matdes.2020.109399
31. Qi F, Wang C, Peng S et al (2021) A co-dispersed nanosystem from strontium-anchored reduced graphene oxide to enhance bioactivity and mechanical property in polymer scaffolds. Mater Chem Front. https://doi.org/10.1039/D0QM00958J
32. Wei D, Zhou Y, Jia D et al (2008) Chemical treatment of TiO_2-based coatings formed by plasma electrolytic oxidation in electrolyte containing nano-HA, calcium salts and phosphates for biomedical applications. Appl Surf Sci 254(6):1775–1782. https://doi.org/10.1016/j.apsusc.2007.07.144
33. Xu YC, Wang ZX, Cheng XQ et al (2016) Positively charged nanofiltration membranes via economically mussel-substance-simulated co-deposition for textile wastewater treatment. Chem Eng J 303:555–564. https://doi.org/10.1016/j.cej.2016.06.024
34. Ghorbani F, Zamanian A, Behnamghader A et al (2019) Bone-like hydroxyapatite mineralization on the bio-inspired PDA nanoparticles using microwave irradiation. Surf Interf 15:38–42. https://doi.org/10.1016/j.surfin.2019.01.007
35. Huan Y, Zhang X, Song J et al (2018) High-performance piezoelectric composite nanogenerator based on Ag/(K, Na) NbO_3 heterostructure. Nano Energy 50:62–69. https://doi.org/10.1016/j.nanoen.2018.05.012
36. Chen K, Xie K, Long Q et al (2017) Fabrication of core–shell Ag@ pDA@ HAp nanoparticles with the ability for controlled release of Ag+ and superior hemocompatibility. RSC Adv 7(47):29368–29377. https://doi.org/10.1039/C7RA03494F

37. Zhang J, Xiao D, He X et al (2018) A novel porous bioceramic scaffold by accumulating hydroxyapatite spheres for large bone tissue engineering. III: characterization of porous structure. Mater Sci Eng C 89:223–229. https://doi.org/10.1016/j.msec.2018.04.013
38. Shuai C, He C, Qian G et al (2021) Mechanically driving supersaturated Fe–Mg solid solution for bone implant: Preparation, solubility and degradation. Compos B Eng 207:108564. https://doi.org/10.1016/j.compositesb.2020.108564
39. Liang H, Yang Y, Xie D et al (2019) Trabecular-like Ti-6Al-4V scaffolds for orthopedic: fabrication by selective laser melting and in vitro biocompatibility. J Mater Sci Technol 35(7):1284–1297. https://doi.org/10.1016/j.jmst.2019.01.012
40. Fernández-Arias M, Boutinguiza M, del Val J et al (2019) RE-irradiation of silver nanoparticles obtained by laser ablation in water and assessment of their antibacterial effect. Appl Surf Sci 473:548–554. https://doi.org/10.1016/j.apsusc.2018.12.182
41. Zeng J, Xu L, Luo X et al (2021) A novel design of SiH/CeO_2(111) van der Waals type-II heterojunction for water splitting. Phys Chem Chem Phys 23:2812–2818. https://doi.org/10.1039/D0CP05238H
42. Shuai C, Zan J, Deng F et al (2021) Core–shell-structured ZIF-8@PDA-HA with controllable Zinc ion release and superior bioactivity for improving a poly-l-lactic acid scaffold. ACS Sustain Chem Eng 9(4):1814–1825. https://doi.org/10.1021/acssuschemeng.0c08009
43. Chen L, Deng C, Li J et al (2019) 3D printing of a lithium-calcium-silicate crystal bioscaffold with dual bioactivities for osteochondral interface reconstruction. Biomaterials 196:138–150. https://doi.org/10.1016/j.biomaterials.2018.04.005
44. Mao D, Li Q, Bai N et al (2018) Porous stable poly(lactic acid)/ethyl cellulose/hydroxyapatite composite scaffolds prepared by a combined method for bone regeneration. Carbohyd Polym 180:104–111. https://doi.org/10.1016/j.carbpol.2017.10.031
45. McShan D, Ray PC, Yu H (2014) Molecular toxicity mechanism of nanosilver. J Food Drug Anal 22(1):116–127. https://doi.org/10.1016/j.jfda.2014.01.010
46. Shuai C, Liu G, Yang Y et al (2020) A strawberry-like Ag-decorated barium titanate enhances piezoelectric and antibacterial activities of polymer scaffold. Nano Energy 74:104825. https://doi.org/10.1016/j.nanoen.2020.104825
47. Kim JS, Kuk E, Yu KN et al (2007) Antimicrobial effects of silver nanoparticles. Nanomed Nanotechnol Biol Med 3(1):95–101. https://doi.org/10.1016/j.nano.2006.12.001
48. Zhu X, Wu D, Wang W et al (2016) Highly effective antibacterial activity and synergistic effect of Ag–MgO nanocomposite against *Escherichia coli*. J Alloys Compd 684:282–290. https://doi.org/10.1016/j.jallcom.2016.05.179
49. Wang Z, Liu S, Ma J et al (2013) Silver nanoparticles induced RNA polymerase-silver binding and RNA transcription inhibition in erythroid progenitor cells. ACS Nano 7(5):4171–4186. https://doi.org/10.1021/nn400594s
50. Zou Z, Liu W, Cao L et al (2020) Advances in the occurrence and biotherapy of osteoporosis. Biochem Soc Trans 48(4):1623–1636. https://doi.org/10.1042/BST20200005
51. Hollister SJ (2005) Porous scaffold design for tissue engineering. Nat Mater 4(7):518. https://doi.org/10.1038/nmat1421
52. Zou A, Liang H, Jiao C et al (2021) Fabrication and properties of $CaSiO_3$/ $Sr_3(PO_4)_2$ composite scaffold based on extrusion deposition. Ceram Int 47(4):4783–4792. https://doi.org/10.1016/j.ceramint.2020.10.048
53. Yang W, Han W, He W et al (2016) Surface topography of hydroxyapatite promotes osteogenic differentiation of human bone marrow mesenchymal stem cells. Mater Sci Eng C 60:45–53. https://doi.org/10.1016/j.msec.2015.11.012
54. Tang W, Lin D, Yu Y et al (2016) Bioinspired trimodal macro/micro/nano-porous scaffolds loading rhBMP-2 for complete regeneration of critical size bone defect. Acta Biomater 32:309–323. https://doi.org/10.1016/j.actbio.2015.12.006
55. Shuai C, Yu L, Feng P et al (2020) Organic montmorillonite produced an interlayer locking effect in a polymer scaffold to enhance interfacial bonding. Mater Chem Front 4(8):2398–2408. https://doi.org/10.1039/D0QM00254B
56. Xia L, Lin K, Jiang X et al (2013) Enhanced osteogenesis through nano-structured surface design of macroporous hydroxyapatite bioceramic scaffolds via activation of ERK and p38 MAPK signaling pathways. J Mater Chem B 1(40):5403–5416. https://doi.org/10.1039/C3TB20945H
57. Wang C, Liu D, Zhang C et al (2016) Defect-related luminescent hydroxyapatite-enhanced osteogenic differentiation of bone mesenchymal stem cells via an ATP-induced cAMP/PKA pathway. ACS Appl Mater Interface 8(18):11262–11271. https://doi.org/10.1021/acsami.6b01103